SURFACE APPEARANCE OF PLUTO AND CHARON

MARC W. BUIE
Lowell Observatory

ELIOT F. YOUNG
NASA Ames Research Center

and

RICHARD P. BINZEL
Massachusetts Institute of Technology

Though the planet is small in size, much work has revealed at least crude glimpses of the surface of Pluto, and to a lesser degree the surface of Charon. The surface of Pluto is seen to be highly variegated and is quite likely a dynamic surface, despite its extreme distance from the Sun and extremely cold surface temperature. We review and discuss the observations and techniques used to create surface albedo maps, compare different map solutions, and discuss their implications.

I. RATIONALE AND USES FOR MAPS

Any planetary surface provides a fundamental record of the history and evolution of the body. Cratering records on older surfaces provide insight into the bombardment records in the early solar system. Weathering patterns provide evidence for the style and strength of erosional processes. Other, more extreme, features are seen when active geological processes are present. Unfortunately, direct imaging of geological processes on Pluto and Charon will have to wait for a spacecraft flyby.

Despite their lower spatial resolution, telescopic observations can provide useful characterizations and predictions about the surfaces of Pluto and Charon. From spectroscopic observations and a fortuitous stellar occultation, Pluto's surface is known to be dominated by volatiles that migrate on the surface. By constructing even crude maps, we can thus constrain the broad volatile distribution since newly deposited frosts are known to be intrinsically more reflective. In a simplistic view, reflectivity is inversely proportional to age—bright regions must be young and dark regions can be much older. Knowledge of albedo domains on the surface can also be combined with thermal and atmospheric models to form the basis of seasonal weather predictions.

Before we can trust any of these higher order results, we must first derive and agree on the basic appearance of Pluto and Charon. In this chapter, we will look at the work completed to date concerning the visual appearances of Pluto and Charon. Most of the work will focus on Pluto, being the larger body, but some results do exist for Charon as well.

II. FUNDAMENTAL LIMITATIONS

A. General Considerations

Aside from our Moon and Mars, groundbased observations have not yielded much detailed information about planetary surfaces other than bulk properties. The primary limitation is one of resolution. Most objects are far enough from Earth that resolution even in the best cases (such as Hubble Space Telescope in low Earth orbit) is not sufficient to resolve surface markings. There has been only one case of a satellite for which resolved albedo domains were derived prior to a spacecraft encounter. Saturn's eighth satellite, Iapetus, was mapped through the inversion of rotational lightcurves (Morrison et al. 1975). These maps were later verified by Voyager. However, in this case, the derivation of the albedo domains was made possible by the extreme contrast on the surface. Lower contrast domains are much harder to map in this way.

The surfaces of Pluto and Charon are among the hardest to image directly. Their angular sizes at perihelion are 0.1 and 0.05 arcsec, substantially smaller than a typical seeing disk from groundbased telescopes. Hubble Space Telescope (HST) with the Faint Object Camera (FOC) can resolve both objects but the spatial resolution is limited.

Mapping of the surfaces of Pluto and Charon has so far been limited to lightcurve inversion techniques. Direct mapping from HST images is still in progress and promises to provide maps similar in quality to the best areas in the lightcurve maps once all the instrumental effects are fully understood. Mapping the surfaces of Pluto and Charon have evolved from simple spot models to more sophisticated finite element maps.

Lightcurve inversion mapping for Pluto and Charon can work better than they did for Iapetus for two reasons. First, the obliquity of Pluto is much higher allowing a much larger variation in sub-Earth latitude as the system orbits the Sun. Over a long enough span of time, it is possible to isolate different latitudes on Pluto as the aspect changes. This advantage comes at a price though. To get a complete set of viewing angles, one must observe the system over a span of 125 years, or half an orbit. Figure 1 shows a plot of the sub-solar latitude on Pluto. Lightcurve observations of the system began in 1954 but the coverage is not particularly complete. Even so, taking this to be a starting point, we need to observe until 2030 before a full span of latitude is covered.

The other reason we can better map Pluto is due to the presence of Charon. As our vantage point passed through the plane of Charon's orbit, we watched as first Charon passed in front and then 3.2 days later passed behind Pluto

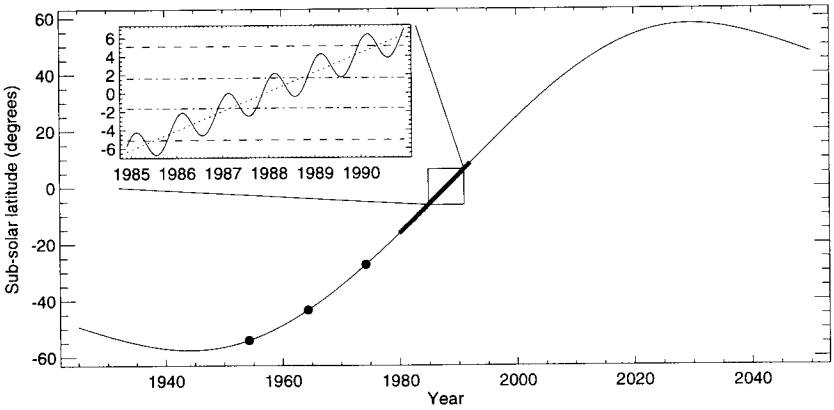

Figure 1. Sub-solar latitude on Pluto from 1925 to 2050. The three dots on the curve indicate where early rotational lightcurves were collected. The thicker portion of the curve shows where more intensive measurements have been made of the lightcurve. The inset expands on the time during which mutual events occurred. The dash–dot line marks the limits of total events and the dashed curve indicates the limits of partial events. The short dash curve is again the sub-solar latitude and the superimposed sinusoidal solid line shows the sub-Earth latitude.

with the cycle repeating with each revolution of Charon. By observing a large number of events all with different geometries, it is possible to infer surface albedo patterns on the eclipsed hemispheres. The inset in Fig. 1 highlights the duration of mutual events just past.

An additional complication in the inversion of lightcurve observations is in decoupling the photometric contributions of Pluto and Charon. Most groundbased measurements are confined to observing the combined light from the system and thus it is impossible to know the individual magnitudes at times other than at total eclipses. The HST, with its high angular resolution imaging capabilities, can easily separate Charon from Pluto. Buie et al. (1996) have finally extracted separate lightcurves and phase coefficients but these results have not yet been incorporated into any surface maps. Such improvements are still in progress.

B. Speed of Event vs Brightness: Implications of S/N

The geometry and dynamics of the Pluto-Charon system place some fundamental limits on what can be achieved through the inversion of mutual event lightcurves. The velocity of Charon relative to Pluto on the plane of the sky at time of minimum separation is 13.4 km/min. Therefore, the leading limb of Charon advances across Pluto at this speed. The best photometric measurements ($\sigma \sim 0.003$ mag) of the mutual events have a time resolution approaching 1 min. Thus the resolution possible from the inversion of such data cannot be much better than 10 km in longitude. The resolution in latitude will be several times worse, because each successive swatch covered or uncovered by Charon is a tall, thin, banana-shaped region on Pluto. Further-

more, even one-minute integrations are too noisy to be inverted into maps; some additional binning is required. What signal-to-noise (S/N) ratio would be required to invert a lightcurve with 1-min resolution? The fractional area covered or uncovered in one minute is about one thousandth of Pluto's disk area. To measure the flux from that thin swatch to one part in five would require a S/N of 5000, which is beyond the best mutual event lightcurves. In practice, the spatial resolution of the maps reviewed here lies between 250 and 500 km. This resolution stands to improve as all of the various data sets are combined into cooperative modeling efforts.

C. Occultation Patterns

The entire season of mutual events as viewed from the Earth lasted from December 1984 to October 1990. The sub-solar latitude slowly and monotonically increased from just south of the equator to the north, crossing the equatorial plane of Pluto on 1987 Dec 12.35. The sub-Earth latitude varies about the sub-solar latitude but changes in a sinusoidal fashion from the parallactic motion caused by the orbital motion of the Earth. The continuing interplay between the relative motions of the Earth and Pluto around the Sun provided a unique geometry for each and every mutual event between Pluto and Charon.

Events occur whenever Pluto's sub-solar ($\delta_\odot$) or sub-Earth ($\delta_\oplus$) latitude satisfies the relation

$$|\delta| < \arcsin\left(\frac{r_p \pm r_c}{d}\right) \tag{1}$$

where r_p is the radius of Pluto, r_c is the radius of Charon, and d is the orbital separation. The plus sign holds for the condition of partial overlap and the minus sign holds for the condition of total overlap.

Prior to the onset of the events, the radii and the orientation of Charon's orbit were not known well enough to predict the onset very accurately. From the orbit solutions we have now, we know very well when the events began and ended. The inset in Fig. 1 shows the sub-solar and sub-Earth latitude during the event season. The horizontal dashed lines are the latitude constraints assuming nominal numbers for the radii of Pluto and Charon. If the sub-solar latitude is between the two dashed lines, the shadow of the foreground object will be cast on the background object at the time of minimum apparent separation. If the sub-Earth latitude is between the dashed lines, then there is overlap between the bodies and part of the background object will be hidden from view.

The duration of total eclipses was much shorter than the partial phases and started and stopped throughout the season. The total eclipses were contained within 1987 and 1988 and were a very busy time for most observational programs that permitted a number of unique experiments. The most important use of the total events was to make measurements of Pluto without contamination of light from Charon. In this way, individual albedos, colors, and spectra were obtained from 0.3 to 2.5 μm.

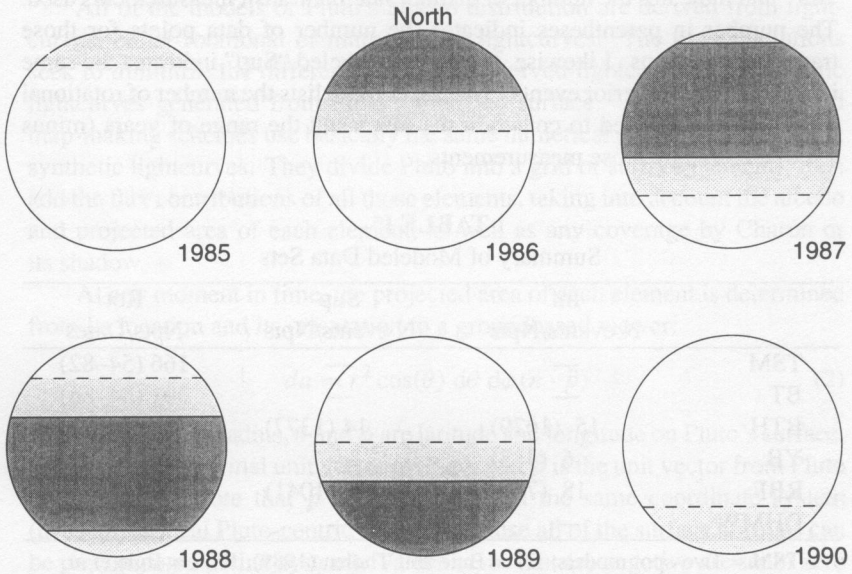

Figure 2. Schematic location of obscured terrain on Pluto during the mutual events. For each year (apparition) during the mutual event season there is one diagram. The dark shaded regions show the range of latitudes covered by a single satellite transit at opposition. The lighter shaded areas show the complete range of obscured areas during the apparition.

Figure 2 depicts the projected limits of shadow and obscuration of Charon on Pluto for each apparition of Pluto during the mutual event season. The constant interplay between shadow and overlap forms the foundation of the mapping process for inverting lightcurves to derive maps. The initial events obscured only the northern hemispheres of Pluto and Charon. As the season continued, the obscured regions slowly shifted to the south. Toward the end of the season, the events stopped briefly at opposition. Events from this time frame are particularly constraining for the radii and help provide even firmer limits.

III. MODELED DATA SETS

There are three principal groups of data that have thus far been modeled to reveal surface albedos. These data sets come from observations at Mauna Kea, McDonald Observatory, and ESO facilities. Other data exist and are as yet unmodeled. Eventually, all wavelength observations and all sites should be utilized to reveal the best possible maps of the surfaces of Pluto and Charon. A summary of the mutual event and other photometric monitoring as they have been published in lightcurve analysis papers appears in Table I. The first column identifies the data set or modeling effort. The second column is labeled

"Inf" and indicates the number of distinct satellite transit measurements used. The number in parentheses indicates the number of data points for those transit observations. Likewise, the column labeled "Sup" indicates the same information for superior events. The last column lists the number of rotational lightcurve points used to constrain the maps and the range of years (minus 1900) covered by those measurements.

TABLE I[a]

Summary of Modeled Data Sets

	Inf N events/Npts	Sup N events/Npts	Rot Npts/Dates
TSM	—	—	166 (54–82)
BT	—	—	301 (54–86)
BTH	15 (1679)	14 (1377)	318 (54–86)
YB	6 (483)	—	—
RBF	18 (748)	15 (1041)	164 (82–90)
DHMW	—	—	210 (54–86)

[a] TSM = Two-spot models; BT = Buie and Tholen (1989); BTH = Buie et al. (1992); YB = Young and Binzel (1993); RBF = Reinsch et al. (1994); DHMW = Drish et al. (1995).

It is of some historical interest to note that the mutual events occurred during an interesting period of transition in astronomical instrumentation, namely the transition from photomultiplier tubes (PMTs) to solid state imaging devices (CCDs). Most observers who started monitoring the Pluto rotation lightcurve in the early 1980s using PMTs chose to stick with the same instrumentation throughout the series for the purpose of consistency. Also through the mid-1980s, most observers could extract higher photometric precision from PMTs than from CCDs. Today with lower read noise and cosmetically excellent CCDs, their photometric precision equals or exceeds that which can be obtained by PMTs. Had the events started some 5 to 10 years later, it is quite likely that most data would have been taken with CCDs and the amount and quality of data could have been higher.

IV. TECHNIQUES

Many different approaches have been used to invert the photometric record of Pluto's lightcurve and infer the surface appearance. Despite admonitions from Russell (1906) that lightcurve inversion is an ill-posed problem, many efforts have been made to do just that. Unique or not, the maps revealed from these efforts elucidate important generic characteristics of Pluto's surface that quantify our intuitive interpretations of the observed lightcurve. In this section, we review the variety of formalisms used in the search for maps of the surface. At the end of each subsection, we will show the maps from each effort.

All of the models of Pluto's albedo distribution are derived from lightcurves, either rotational or mutual event lightcurves. The model solutions seek to minimize the difference between observed lightcurves and synthetic lightcurves generated from Pluto's modeled surface. All of the published map-making schemes use basically the same numerical procedure to generate synthetic lightcurves. They divide Pluto into a grid of surface elements, then add the flux contributions of all those elements, taking into account the albedo and projected area of each element, as well as any coverage by Charon or its shadow.

At any moment in time, the projected area of each element is determined from its location and its orientation to a groundbased viewer:

$$da = r^2 \cos(\theta)\, d\theta\, d\phi(\hat{n} \cdot \hat{p}) \tag{2}$$

where r is Pluto's radius, θ and ϕ are latitude and longitude on Pluto's surface, $\hat{n}$ is the surface normal unit vector at (θ,ϕ), and $\hat{p}$ is the unit vector from Pluto to the Earth. Note that $\hat{p}$ and $\hat{n}$ must be in the same coordinate system (usually the local Pluto-centric system, because all of the surface normals can be precomputed in that system). Values of da that are negative are set to zero because they represent elements that do not contribute to Pluto's flux, being on Pluto's far side. Some surface elements will be blocked by Charon or its shadow; the areas of these elements are also set to zero.

Most modelers have assumed that surface fluxes do not depend on viewing geometry. The exception is the maps by Buie et al. (1992), which use bidirectional reflectances to describe the surface flux. The advantage of the perspective-independent surface flux treatment is that Pluto's total flux at any moment is a linear combination of unknowns (i.e., the surface fluxes), whereas the bidirectional reflectance treatment, being nonlinear, requires an iterative scheme to converge to a solution. The disadvantage is that a surface element's flux may be overestimated when it happens to be near the limb. The chapter Appendix compares the linear case with various Minnaert limb parameters to the bidirectional reflectance case.

The goal of each mapping scheme is to find the set of surface albedos that provides the best match to the observed lightcurves. A typical least squares map-fitting scheme might proceed as follows:

1. Subdivide Pluto's surface into discrete elements.
2. Nonlinear models only: initialize the elements, perhaps by assigning the average Pluto albedo to each element.
3. For each point in the observed lightcurve data set, generate a synthetic flux from the current model of Pluto's surface. This step requires an accurate model of the system geometry.
4. Adjust the surface parameters to minimize the difference between the synthetic and observed lightcurves. If the model for Pluto's reflected flux is linear, one iteration will yield a solution. For nonlinear models (such as a Hapke bidirectional reflectance model), the parameters are updated and

step 3 is repeated until the surface solution converges. The quantity to be minimized is usually the weighted sum of squared differences between the observed and synthetic lightcurves.

This procedure seems straightforward. Here's what is likely to go wrong if you follow these steps:

Subdivisions are too fine. If the available lightcurve data do not provide sufficient spatial resolution, pairs of adjacent surface elements are likely to have highly correlated solutions. You might know the sum of their reflected fluxes, but not their individual fluxes.

Lightcurves are too noisy. Noisy lightcurves, combined with small pixels, can lead to especially interesting results. For example, lightcurves should decrease monotonically during the initial eclipse ingress, as Pluto's exposed area decreases. Any positive noise spike during this part of the event translates to a negative albedo on Pluto's surface, usually with a neighboring region that is extremely bright.

The solution to both of these problems is smoothing, which reduces the spatial resolution. Except for the spot models, all of the maps in this chapter rely on smoothing.

A. Spot Models

Spot modeling of the surface of Pluto refers to a simplistic model where deviations in albedo from the mean, or background albedo, are confined to a circular region (spot). This approach was originally developed and is still used to model star spots on certain variable stars (cf., Eaton and Hall 1979). This technique is useful in that it permits a fast, analytical, evaluation of the reflected flux from the surface at any orientation. When applied to Pluto, this process should be easier than for starspots since we presume the surface features on Pluto are largely static with time. Furthermore, a spot is characterized by relatively few free parameters; latitude and longitude of center, size or radius, and albedo plus any other photometric parameters needed for this domain.

Marcialis (1983) was the first to apply spot modeling to the study of Pluto's lightcurve (this work will hereafter be referred to as TSM, for two-spot model). In the TSM, each spot is characterized by a location (latitude, longitude), radius, and a normal albedo. Limb-darkening was also used but $x = 0.5$ was forced on the model (see Appendix A for limb-darkening definitions and discussion). The TSM modeled the normalized lightcurves for their amplitude and shape with two dark spots near the equator. A separate model with two polar caps was constructed to explain what was termed "secular dimming" for the drop in intrinsic geometric albedo between 1954 and 1980. Marcialis also used the modeling to attempt an improved value for the linear phase coefficient for Pluto but no provision was made for different values between Pluto and Charon. Figure 3 shows the TSM map and the band model

reprojected onto a rectangular map. This projection distorts the shape of the circular spots.

The model of Buie and Tholen (1989) (hereafter referred to as BT) improved on the TSM with several important differences: (1) increased data set with the timebase extended to 1986; (2) the incorporation of Hapke (1981) reflectance theory; and (3) modeling of data as absolute photometry, not relative. The adoption of the Hapke theory eliminates the limb-darkening coefficient in favor of other quantities that control reflectance. Also, use of the Hapke function allows the model to directly account for the solar phase angle without the need for a linear phase coefficient as was the case for the Marcialis model. The unknowns in this case are the average particle single scattering albedo and phase function and the surface compaction parameter. The switch to modeling absolute photometry is fundamentally more important. In this step, all spots were fitted against the photometry simultaneously and forced to reproduce the absolute photometry. This left the model sensitive to non-physical model parameters (i.e., single scattering albedo must be between 0 and 1, inclusive). Figure 4 shows two maps for Pluto that matched the rotational lightcurve data between 1954 and 1986.

Both models used a pure least-squares fitting procedure. As described by Russell, these maps cannot return a unique answer for the inversion problem. Indeed, the work by Buie and Tholen (1989) found two equally likely spot configurations that reproduced the data at that time. Nonetheless, these works both showed that a static albedo model was capable of explaining the general orbital and rotational lightcurves. Finally, both models assumed a constant flux contribution from Charon with solar phase angle variations that were equal to that for Pluto.

B. Maximum Entropy Reconstruction

As was pointed out earlier, all the aforementioned techniques provide a solution based on minimizing χ^2 that is not unique. In general, the problem of non-uniqueness worsens as the number of free parameters increases and becomes much more serious for any finite element approach to modeling.

The technique of maximum entropy reconstruction (MaxEnt) attempts to eliminate the non-uniqueness difficulty by adding an additional constraint to typical least squares methods. As implemented by Buie et al. (1992), the MaxEnt process is an extension of the finite element model. The model flux is computed from a gridded surface and the data constraint is quantified with the familiar merit function,

$$\chi^2 = \frac{1}{M} \sum_{k=1}^{M} \left(\frac{d_k - f_k}{\sigma_k} \right)^2 \tag{3}$$

where d_k and f_k are the observed and predicted data, and σ_k is the measured or estimated uncertainty of d_k. The data constraint requires $\chi^2 = C_{\text{aim}}$ which imposes a specific goodness-of-fit constraint on the data.

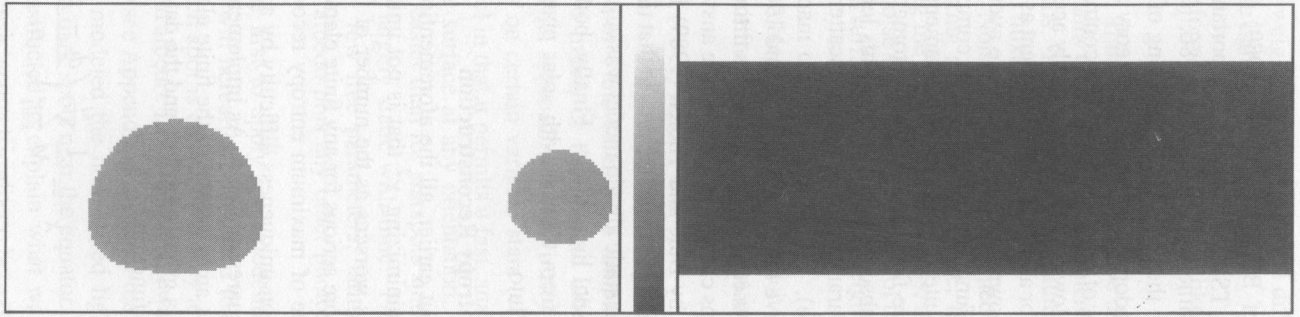

Figure 3. Map of the surface of Pluto from Marcialis (1983). These are two rectangular projections of the albedo distributions proposed in the TSM. The left map is the two spot configuration that reproduces the relative photometry from 1954–1982. The spots are no longer circular because of the projection. The right-hand map is the band model proposed to account for the orbital lightcurve. Both maps show normal albedo (albeit relative) ranging from 0 (black) to 1 (white). North is at the top, 0 degrees east longitude is at the left edge of the map, and east longitude increases to the right.

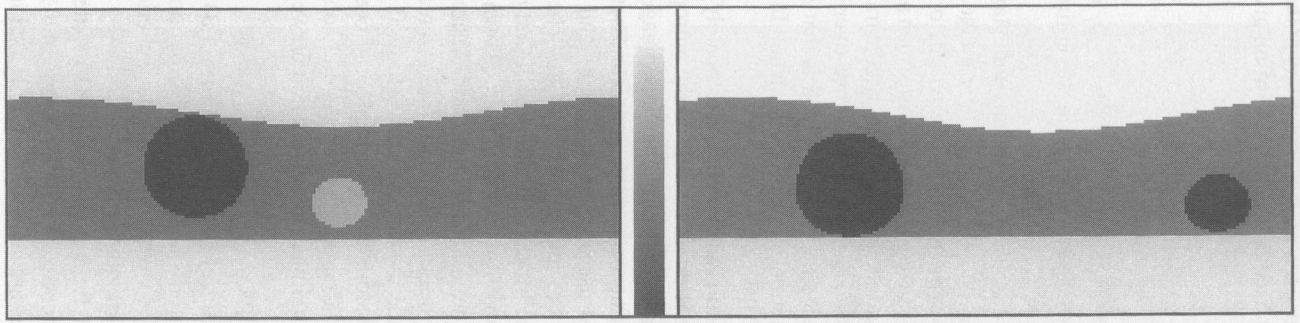

Figure 4. Two proposed maps of Pluto from Buie and Tholen (1989). After the nomenclature in that work, the left model is SHELF (preferred) and the right-hand model is MAX. These images are in bi-directional reflectance divided by π at zero degrees phase angle (which is equivalent to normal albedo). The image values range from 0 (black) to 1.5 (white). The map orientation is the same as the previous figure.

To this familiar constraint, MaxEnt adds the constraint of requiring the solution to also maximize the entropy in the model image (tiled surface). Buie et al. (1992) used an entropy definition given by

$$S = \sum_{j=1}^{N} I_j - D_j - I_j \cdot \ln\left(\frac{I_j}{D_j}\right) \tag{4}$$

where I_j is the image value at tile j, D_j is the corresponding default value, and N is the number of tiles in the entire model image (Pluto and Charon combined).

Given these two constraints, the MaxEnt method maximizes S subject to $\chi^2 = C_{\text{aim}}$ and returns a unique image. One additional advantage of this method is that the model image will be optimally balanced between entropy and the data. Strong data constraints such as those on the eclipsed hemispheres will be little affected by the entropy constraints. Regions of the surface that are poorly constrained will be smoothed over by the entropy constraint. Another way to describe the MaxEnt result is that it provides a map with just enough spatial resolution to explain the data. In regions of poorer constraints the resolution will be reduced.

The default image D is (unfortunately) crucial to the MaxEnt reconstruction because it directly controls the entropy function. The other techniques require smoothing and this default image is a manifestation of smoothing for the MaxEnt method. A complete discussion of the details governing the selection and use of a default image and other details regarding the use of MaxEnt are beyond the scope of this chapter and the reader is encouraged to consult the more complete description provide by Buie et al. (1992). The resulting maps from this effort are shown in Fig. 5 where the map of Pluto appears on the left and the map of Charon appears on the right. Some artifacts appear in these maps that are not real. The vertical stripes at 90° and 270° longitude are always on the limb at the time of mutual events and are apparently distorted in the inversion process. Also the bright regions at the south pole of Charon at half of the map longitudes are not real and are caused by incomplete lightcurve separation between Pluto and Charon.

C. MIT Maps

Young and Binzel (1993; henceforth YB) fit three separate models to solve for Pluto's sub-Charon albedo distribution. These three models represented Pluto's surface with finite elements, spherical harmonics, and polynomials of latitude and longitude.

The YB finite element model divides Pluto into a 6×6 grid of tiles. Each tile extends 30 deg in latitude and 32.5 deg in longitude. The polar and limb tiles are severely foreshortened in this scheme, and their errors are unreasonably high. Some of the tiles have negative albedos, and some (usually adjacent) albedos are greater than one. No attempt was made to constrain the parameters to the range from 0 to 1 in the fit. Instead, the resulting map was

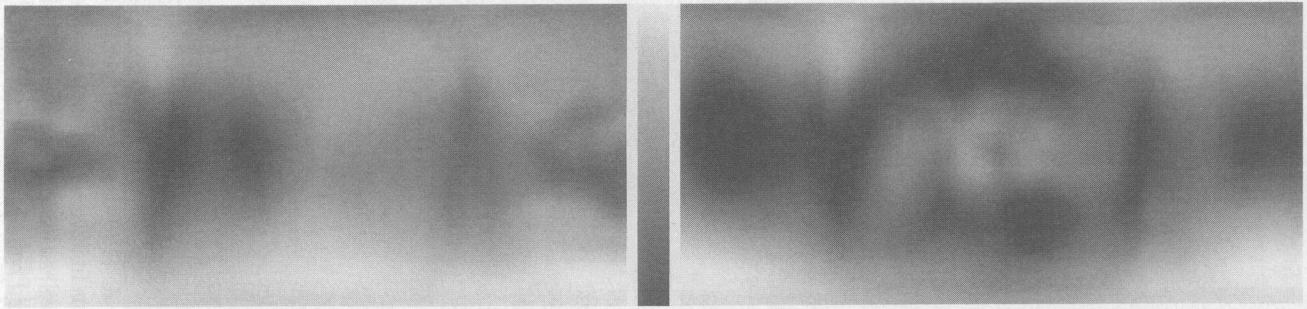

Figure 5. MaxEnt maps of Pluto and Charon from Buie et al. (1992). The map on the left is of Pluto, and Charon is on the right. As for the BT maps, the maps have been converted to normal albedo for purposes of comparison and range between 0 (black) and 1.2 (white). The relative scaling between Pluto and Charon has been preserved. The map orientations are the same as those in Fig. 4.

smoothed in the spatial domain with an adaptive Gaussian-shaped filter. The width of this filter is inversely proportional to the error of the pixel being smoothed. A filter width corresponding to roughly 400 km at Pluto's equator eliminates all of the illegal albedos. The reduced χ^2 for this map is 2.01, based on 483 points from six different mutual event lightcurves.

The spherical harmonic and polynomial maps decompose Pluto's surface into a linear combination of functions of latitude and longitude. Finite elements are also functions of latitude and longitude; they just happen to be zero everywhere except under a certain region, where they evaluate to one.

The procedure for finding the spherical harmonic representation of Pluto's surface, like the finite element case, minimizes the differences between modeled and observed lightcurves. The mutual event lightcurves do not support maps of infinite spatial resolution, nor do they support an infinite number of spherical harmonic terms. YB use a spherical harmonic series truncated at $Y_{66}(\theta, \phi)$. A linear least squares fit for a subset of spherical harmonic coefficients yields a map with a χ^2 of 1.82.

The polynomial functions used by YB are of the form

$$s(\theta, \phi) = \sum a_{nm} P_{nm}(\theta, \phi) \text{ and} \tag{5}$$

$$P_{nm}(\theta, \phi) = \theta^n \phi^m. \tag{6}$$

YB used polynomial terms up through P_{88}. It is important to note that neither the polynomials nor the spherical harmonics form an orthogonal basis set over the region of support (Pluto's sub-Charon hemisphere). Many distinct spherical harmonic or polynomial terms cannot be fit without being highly correlated to other terms of different orders. In both the spherical harmonic and polynomial cases there are families of highly correlated terms. YB dealt with correlated parameters by removing the higher-order term from a fit whenever a pair of terms had cross correlations over 0.95. The polynomial map has a reduced χ^2 of 1.53.

The spatial resolution of all three maps is approximately 400 km. YB generated synthetic lightcurves from several imaginary Plutos, each having surface features of various sizes. Gaussian-distributed noise matching the original data sets was added to the synthetic lightcurves. The reconstructions were able to recover features 500 km in extent, but not ones that were 250 km. The map of the eclipsed hemisphere of Pluto is shown in Fig. 6.

D. ESO 17-Tile Map

Reinsch et al. (1994; henceforth RBF) used rotational and mutual event lightcurves to fit several physical and orbital parameters of the Pluto–Charon system, as well as longitudinally resolved maps based only on rotational lightcurves and a 17-tile map of Pluto's sub-Charon hemisphere based on mutual event lightcurves. Their finite element map consists of five bands in latitude, all of which are divided longitudinally into five tiles except for the northern- and southernmost bands, which are not subdivided longitudinally at all. The

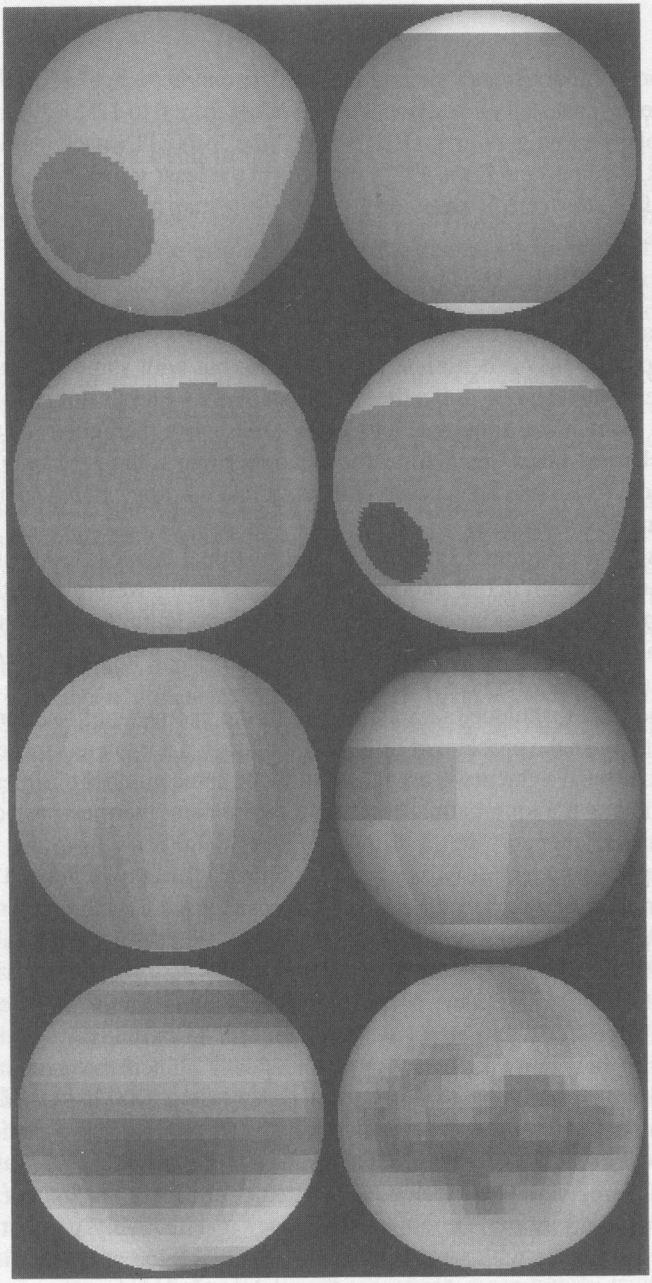

Figure 6. Comparison of sub-Charon hemisphere of Pluto from different models. The top two images correspond to the TSM from Fig. 3. The second row are the SHELF and MAX maps from Fig. 4. The left side of the third row is the DHMW map. The right side is the RBF map. The left side of the last row is the YB map. The right side is the BTH map. All of the images are in normal reflectance units with limb-darkening as indicated by each modeler. The images have also been scaled so that the total reflectance from each image is the same for all.

location of subdivisions is determined by Charon's coverage. Most of the tiles have been sized so their fractional errors range from 6 to 12% of their albedos (the poles have higher errors). RBF used the MINUITS package developed at CERN (James and Roos 1975) to perform the least squares fits. Using 907 points from thirteen different events, the 17-tile map has a reduced χ^2 of 1.09 and is shown in Fig. 6.

E. MLI Map

The matrix lightcurve inversion (MLI) map presented by Drish et al. (1995; henceforth DHMW) is a finite element map, but with some interesting differences. Most significantly, the MLI map divides Pluto's entire sphere into 40×25 elements in longitude and latitude, far more than either of the other finite element maps. Unlike most of the other maps, the MLI map is based solely on rotational lightcurves, and fits Pluto's entire sphere, not just the sub-Charon hemisphere.

As Russell pointed out in 1906, a rotational lightcurve constrains an albedo distribution in one dimension only. Despite his warnings, with several rotational lightcurves taken at different sub-Earth latitudes, it becomes possible to achieve resolution in latitude and longitude, provided the S/N of the data is sufficiently high.

The MLI technique takes advantage of the geometry of rotational lightcurves to make the problem of fitting 1000 unknown parameters more tenable. If the rotational lightcurves are rebinned to the same number of timesteps per revolution as the longitudinal resolution of the map, then the projected area of a surface element (da) is the same as its neighbor's from the previous timestep. The general least squares design matrix usually requires a separate row for each timestep to describe the exposed area of each element at that timestep (Young and Binzel 1993), but the MLI algorithm produces a design matrix that is made up of circulant submatrices, where each submatrix row is identical to its predecessor except for a shift by one column. In other words, the entire MLI design matrix can be represented by only J rows with no loss in information content, where J is the number of lightcurves used in the fit.

The MLI map has more unknown parameters (1000 tile albedos) than data points, which means that a solution would be nonunique if the design matrix were simply inverted to solve for the parameters. DHMW use Jacobi's method, a regularization technique, to iteratively solve for the parameters. This technique uses a smoothing parameter to effectively group tiles into larger spatial units with related albedos. The smoothing parameter is chosen to be small enough to maintain good spatial resolution, but large enough to avoid any noise-induced artifacts in the maps. During the regularization the albedos are contrained to lie between 0 and 1. Some smoothing also occurs in the lighcurve preprocessing, because the MLI technique interpolates points from the raw lightcurves to get the required periodic spacing in time. (Note that the MLI technique will work with gaps in the input lightcurves.) The portion of the MLI map on the eclipsed hemisphere of Pluto is shown in Fig. 6.

V. MAP COMPARISONS

Figure 6 shows a comparison of the eclipsed hemisphere of Pluto from all published maps. The trend in the figure is a general increase in data constraints and model complexity from top to bottom. Only the most qualitative agreement is expected between the rotational lightcurve maps and the later mutual event maps. The brighter south polar region seems to be favored amongst all models though the spot model requirement of a bright north pole is not strongly confirmed with mutual event maps. The most similar maps in modeled resolution are the YB and BTH maps, shown at the bottom of Fig. 6. A detailed comparison of these maps shows a remarkable agreement in the structure of the south polar and southern mid-latitudes. The agreement is not quite as good in the northern regions but the following discussion may provide a plausible explanation for this discrepancy.

A map can be no better than the data used to constrain it. The effect of the signal-to-noise ratio and time resolution of the photometric observations has a direct bearing on the resolution of the map. The actual coverage attained in a data set also controls the quality of reconstruction possible. To assist in visualizing the constraints provided by one or more events, we have constructed coverage maps. A coverage map shows for each point on the eclipsed hemisphere a measure of how well the pixel is constrained by data. To construct the coverage map, the surface is broken into discrete bins. For each data point we measure a flux and an associated uncertainty. The score, S_{ij}, given to the i^{th} tile is

$$S_{ij} = \frac{B_{ij}(\hat{n}_i \cdot \hat{\mu}_e)(\hat{n} \cdot \hat{\mu}_i)}{a_i \sigma_j} \tag{7}$$

where B_{ij} is 1 if that pixel could be visible but is blocked by either a shadow or physical obscuration, $\hat{n}_i$ is the surface normal unit vector, $\hat{\mu}_e$ is the unit vector toward the observer (Earth), $\hat{\mu}_i$ is the unit vector toward the Sun, a_i is the surface area of the tile, and σ_j is the uncertainty of the measurement. The complete coverage map is thus the sum of S_{ij} over j for one or more data points. This map does not summarize *all* of the constraints provided by the data set but does illustrate what the mutual event data provide.

Figure 7 shows a contour map of the ratio of two coverage maps. Ratioed are the YB map and the BTH map for their respective modeled data sets. Numbers closer to unity indicate similar data constraints. Numbers much less than one indicate areas that are much more poorly constrained. In this case, the northern mid-latitudes are clearly much more poorly constrained in the YB map than in the BTH map. This may account for relatively poor agreement between these maps in this area. There is even a small area in the YB map where there is no mutual event constraint at all because one of the transit events could not be observed past mid-event.

To illustrate the different absolute levels of constraint in each data set, Fig. 8 shows plots cutting the map at different locations. Added to the curves

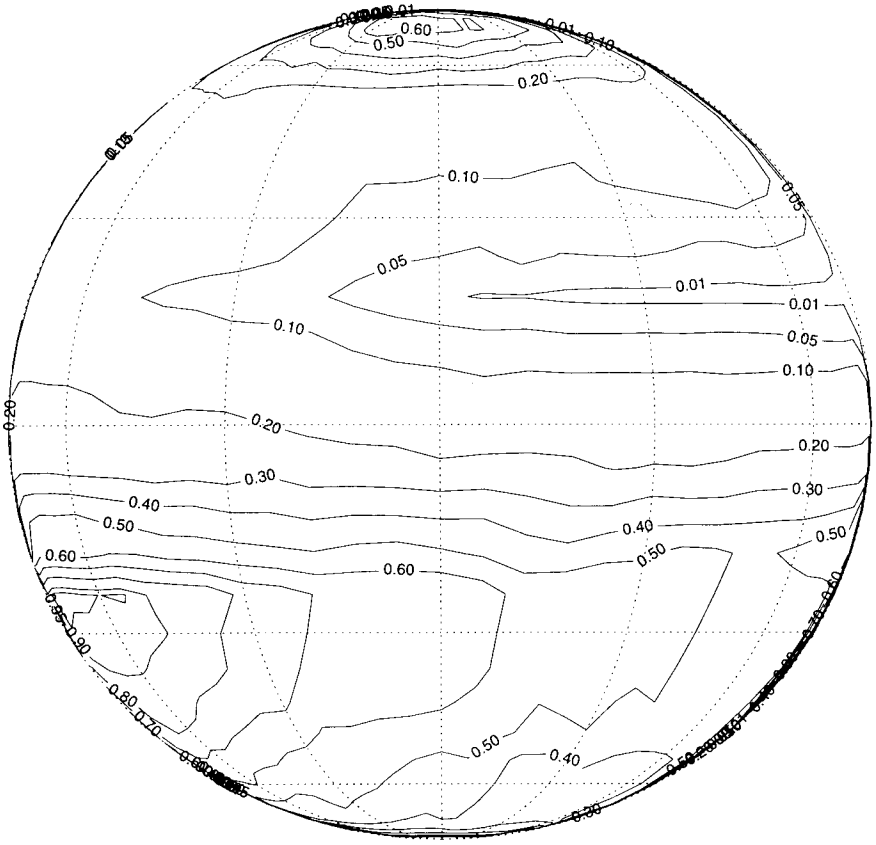

Figure 7. Coverage map ratio between the YB and BTH maps for the sub-Charon hemisphere of Pluto. A value of 1 would indicate equal levels of data constraint in the two maps.

from the YB and BTH maps are traces from the BTH data set if all the available MKO observations were included (an extra dozen events or so). In general, this plot shows that the pole and limb are more poorly constrained compared to the center of the disk. This is caused by the foreshortening of areas near the limb so that when they are covered up the lightcurve is not diminished as much as it is by a similar area near the center of the disk. This figure also shows that the BTH data set is fairly complete but will improve with the addition of more data. For example, the longitude scan at $-60°$ latitude shows that the extra data will increase the constraints by nearly a factor of two. This is to be expected because the transit data from the BTH map had more complete coverage early in the mutual event season when the transits were covering the northern regions.

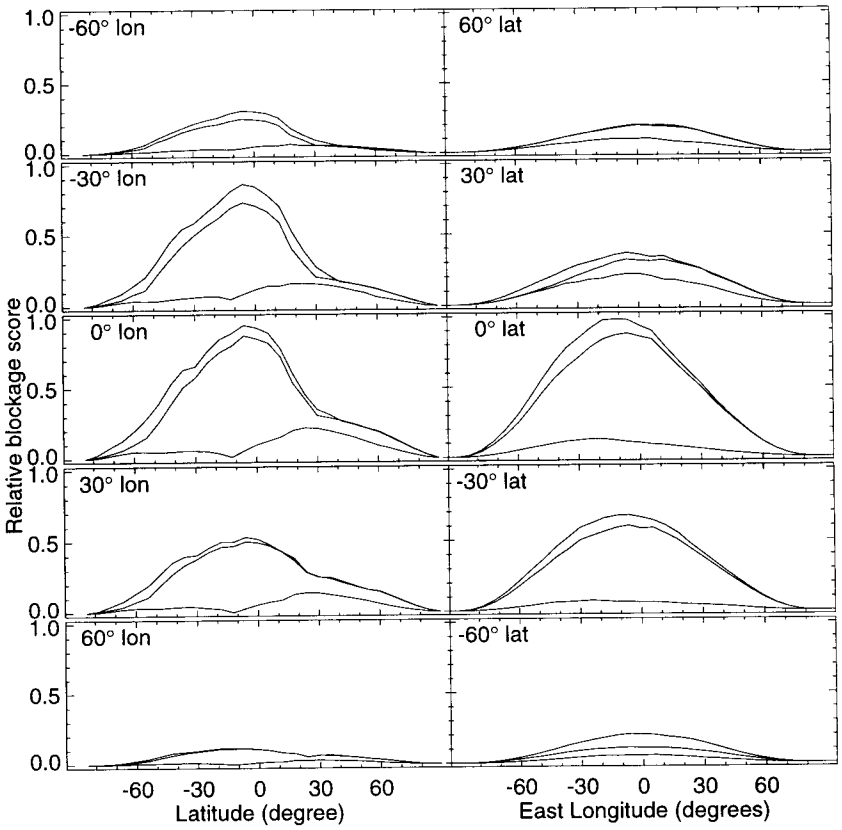

Figure 8. Scans across the coverage maps for YB (lowest curve), BTH (middle curve), and BTH if augmented by all data taken at Mauna Kea (upper curve). The left panel shows latitudinal cuts at different longitudes. The longitudes are shown in the upper left corner of each sub-panel. The right panel shows longitudinal cuts at different latitudes.

VI. COLOR CONSTRAINTS FROM MUTUAL EVENTS

Photometric measurements of mutual event lightcurves performed in more than one filter band (for example B and V) provide the capability to derive individual color information for the surfaces of Pluto and Charon. At present, these data have been analyzed only to the extent that conclusive results are available to describe color distributions at hemispheric scales. Color maps, derived in much the same way as the albedo maps described here, are a forthcoming development.

Averaged over a complete rotation, the average $B - V$ and $V - R$ magnitudes of the Pluto–Charon system were found to be 0.846 ± 0.010 and 0.462 ± 0.021 (Reinsch et al. 1994). During the total occultation events of 1987, Binzel (1988) found that the $B - V$ magnitude of the system increased

(became redder) by 0.024 magnitude as Charon became totally obscured behind Pluto. Qualitatively this implied that Charon must be a bluer (less red) body than Pluto. Quantitatively, Binzel (1988) derived a $B - V$ value of 0.867±0.008 for the anti-Charon hemisphere of Pluto and 0.700±0.010 for the Pluto-facing hemisphere of Charon. Similar measurements reported and analyzed by Reinsch et al. (1994) yield analogous values having excellent agreement: 0.871±0.014 and 0.701±0.014, respectively. Noting that the Sun has a $B - V$ magnitude of 0.65, these measurements imply that Charon has a neutral gray surface compared with the red surface of Pluto. More highly resolved spectra over visible and near infrared wavelengths (see the chapter by Cruikshank et al.) reveal that the color differences arise from distinct compositional differences between Pluto and Charon's surfaces, where Pluto's surface is dominated by nitrogen and methane ice while Charon's appears to be water ice.

Multicolor photometry of the mutual events placed a constraint on the degree of hemispherical color variation on Charon. During transit events of 1987 (the complements of the total occultation events described above), Binzel (1988) found a blue-shift in the $B - V$ color of the system amounting to 0.022 magnitudes which yielded a $B - V$ value of 0.725±0.025 for the color of the outward facing hemisphere of Charon. He concluded that the measures for the two hemispheres were consistent with a uniform color for Charon. These hemispheric results have been confirmed by individually resolved photometric images of Pluto and Charon obtained with the HST. Buie et al. (1996) find a $B - V$ value for Charon of 0.710±0.011 which shows no statistically significant change with longitude. Their individual color measurements for Pluto are also consistent with the mutual event results, where their closest available measurement in longitude ($\lambda = 123°$) yields a $B - V$ color of 0.873±0.002. Pluto, however, does appear to show some color variation with rotation as Buie et al. find a significantly different $B - V$ value of 0.863±0.002 at longitude 289°, suggesting that the darker regions on Pluto are redder in color.

VII. IMPLICATIONS OF MAPS

A. Contrast

One result that all maps agree on is the presence of large variations in albedo from one region to another. Originally postulated from the spot models, subsequent finite element maps confirm this result. The MaxEnt map predicts a contrast ratio of roughly 6 to 1, nearly as high as that observed for Iapetus by Voyager. As discussed by Stern et al. (1988), dark materials are readily explained on Pluto as the result of radiation darkening of CH_4 frosts. The "challenge" is to provide a mechanism that keeps the other portions of the surface bright. The explanation provided by Stern is that the surface is continually (on a time scale shorter than a Pluto year) resurfaced or replenished with fresh frost.

B. Time Variability

An unresolved issue in understanding Pluto's surface is the degree to which it varies with time. The insolation is so low for Pluto that little variation can occur from the 6.4 day rotation period. However, the large variation in heliocentric distance must surely play some role. In addition to suggestions from Stern et al. (1988), thermal models of Pluto also indicate a high degree of volatile migration during the course of a Pluto year (Hansen 1994). Both of these considerations offer compelling reasons to expect change but these changes have yet to be conclusively proven that they have been seen from groundbased observations. With the exception of the DHMW mapping effort, all modelers have been able to reproduce the observed photometric behavior of Pluto with static albedo models. The conclusions of time variability offered by Drish et al. (1995) are tempting but do not account for all observations, being based solely on rotational data but no mutual event observations. The most conclusive tests may come from direct HST images combined with mutual event maps. A more quantitative determination of the level of volatile migration is yet to come but will be of tremendous importance for further constraints on our understanding of the surface.

C. Composition

Great strides have been made in recent years to improve our knowledge of the surface composition of Pluto. Methane has been known to exist since the first measurements by Cruikshank et al. (1976). Further spectroscopic studies have revealed N_2 and CO on the surface (Owen et al. 1993). The presence of very bright regions on the surface of Pluto from these mapping efforts provides a nicely complementary confirmation of fresh volatiles on the surface.

VIII. PROSPECTS FOR FUTURE IMPROVEMENTS

A. Combination of All Mutual Event Data

The work of Buie et al. (1992) is based on the most uniform mutual event and rotational lightcurve coverage work. However, there have thus far been no efforts to model all data sets together. Full use of all events will certainly increase the quality, both in signal-to-noise ratio and spatial resolution, of the maps. Once all data sets are gathered, there should be nearly twice as much data as that modeled by BTH.

B. Simultaneous Orbit and Albedo Fitting

For all the mapping to date, modeling of the surface has always assumed a known geometry that includes orbital parameters and the sizes of Pluto and Charon. Some correlations do exist between the orbit solution and the albedo maps but these effects are expected to be small. Ultimately, as the mapping efforts get more sophisticated and are better able to fit the data there

will be a need to simultaneously fit for the radii and at least some of the orbital parameters.

C. Separate Lightcurve Data Constraints

As mentioned earlier, all the models to date have assumed identical phase coefficients and thus similar surface properties for Pluto and Charon. New observations by Buie et al. (1996) using HST have at last separated the phase coefficients. These results clearly show a difference that will be important to the Charon/Pluto flux ratio for different events. Based purely on the lightcurve and phase coefficient results, the Pluto/Charon flux ratio at superior events ranges from 6.47 to 6.82 between opposition and quadrature. For inferior events, the flux ratio varies between 5.75 and 6.06.

D. Direct HST Imaging Constraints

Another contribution from HST will come from direct imaging of the surface of Pluto. The FOC with the corrective optics provides images with 5 to 6 resolution elements across the disk of Pluto. When fully analyzed, these images can provide direct and instantaneous images of Pluto. One impediment to direct interpretation of the data is that the point-spread function is still important. Even with perfect optics, the transfer function for the telescope is an Airy disk. The spacing between the peak and the first ring is just a little smaller than the disk of Pluto and thus reduces the contrast one would infer from the raw images. To fully realize the information contained in HST images, one must still perform a modeling inversion of the maps, though the problem is not quite as severe as inverting the mutual event lightcurves. The first attempt at this direct mapping has been made by Albrecht et al. (1994) where they conclude that the HST imaging is largely in agreement with the albedo models. Subsequent to the Albrecht observations, a global imaging set was collected by Stern et al. (1996) but detailed comparisons against the models have not yet been completed. Both of these works show that with enough effort, HST can be a very powerful tool in extending our knowledge of the surface of Pluto.

E. Continued Observations

The best approach to a vastly greater understanding and knowledge of the surfaces of Pluto and Charon would clearly be a spacecraft flyby. The current programmatic and funding climate seem to be conspiring to preclude this option so our next best effort would be to continue with diligent observations both from the ground and from HST. These two options are not mutually exclusive. The spatial resolution from HST can be exploited to directly monitor the large-scale migration of volatiles. HST is not well suited, however, to the exacting requirements of the absolute photometry possible from the ground. Therefore, groundbased photometry of the combined light from the system will be needed to accurately monitor the evolution of the orbital and rotational lightcurves and also monitor any shift in surface scattering properties through

changes to the phase coefficients. The next 15 to 20 years will be very important to monitor with photometry as all models predict a rapid evolution of the lightcurve as the Sun moves away from Pluto's equator.

APPENDIX: REFLECTANCES AND ALBEDOS

1. Bi-directional Reflectance (Single-scattering Albedo). The spot model of Buie and Tholen (1989) and the MaxEnt model from Buie et al. (1992) both use the Hapke theory for computing the observed flux from Pluto given certain parameters. Synthetic images of Pluto and Charon are images of bi-directional reflectance which when integrated over the visible disk yield the observed flux. The basic equation for bi-directional reflectance (r) from Hapke (1981) is

$$r(\mu_0, \mu, g) = \frac{w}{4\pi} \frac{\mu_0}{\mu_0 + \mu} \{[1 + B(g)]P(g) + H(\mu_0)H(\mu) - 1\} \tag{8}$$

$$B(g) = B_0(1 - 3|g|/2h) \tag{9}$$

$$B_0 \approx e^{-w^2/2} \tag{10}$$

$$H(\mu) = \frac{1 + 2\mu}{1 + 2\gamma\mu} \text{ and} \tag{11}$$

$$\gamma = (1 - w)^{1/2} \tag{12}$$

where μ_0 is the cosine of the angle from the surface normal for the incident solar flux, μ is the cosine of the emission angle relative to the surface normal, g is the solar phase angle, w is the average particle single scattering albedo, $B(g)$ is the backscatter function (assuming that $g \ll 1$), and $P(g)$ is average single particle phase function. For Pluto mapping, no function has been assumed for $P(g)$ because the range of phase angles observable from Earth is so small.

2. Normal Reflectance: Linear Limb Darkening. In terms of the Hapke equations above, normal reflectance is $\pi r(1, 1, 0)$. In the TSM of Marcialis (1983), linear limb darkening of the form

$$I(\mu) = I_0[1 - x + x\mu] \tag{13}$$

was used. In this case, the variable x is the limb darkening coefficient with $x = 0$ being the case of no limb darkening and $x = 1$ being the case of a Lambert sphere.

3. Normal Reflectance: Minnaert Function. Another formalism used by YB, RBF, and DHMW is the Minnaert function with normal reflectance. For the case of very small phase angles (in this case actually set to zero), the simplified form of the Minnaert limb darkening rule is

$$I(\mu) = I_0\mu^{2k-1} \tag{14}$$

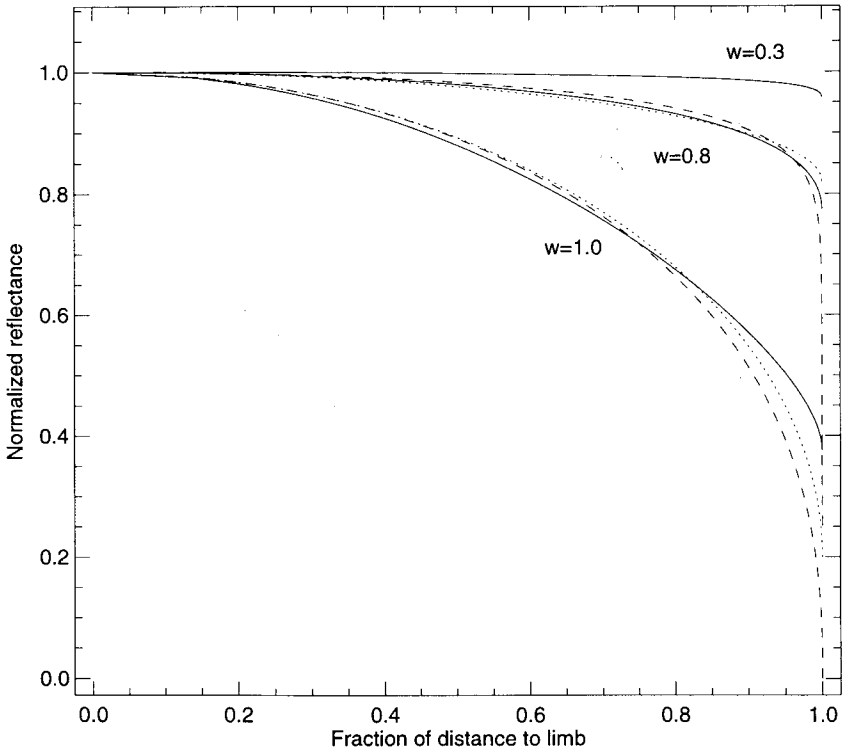

Figure 9. Comparison of center-to-limb brightness profiles between Hapke, Minnaert, and linear-limb darkening scattering models. The solid lines are for the Hapke function. The three curves are computed for $h = 0.3$, $P(0) = 3.0$, and $w = 0.3$, 0.8, and 1.0. Minimal limb-darkening is seen for the low albedo case. The most limb-darkening applies to the highest albedo case. All curves are normalized to 1.0 at the center of the disk. The dotted curves are for the linear limb-darkening formalism. Values of $x = 0.18$ and $x = 0.8$ nearly match the $w = 0.8$ and $w = 1.0$ cases, respectively. The dashed curves are Minnaert curves for $k = 0.56$ and $k = 0.9$ for the same two Hapke cases.

where k is the Minnaert coefficient.

4. Comparison of Limb Darkening Profiles. With a judicious choice of parameters each of these three formulas can be made to exhibit similar center-to-limb profiles as long as one does not get too close to the limb. The Minnaert function (except for $k = 0.5$) always produces a reflectance of zero at the limb. The linear limb darkening formula is intermediate between the Hapke function and the Minnaert function. It does not require zero at the limb but is significantly low approaching the limb. To illustrate these differences, Fig. 9 compares the three functions. The choice of single-scattering albedo is meant to cover the range found in the Pluto MaxEnt map. Note that significant limb-darkening occurs only for very high values of w. It should be clear from

this comparison that the choice of scattering function can affect radii from modeling mutual event data or even modeling of direct images similar to what the HST can collect (see, e.g., Albrecht et al. 1994).

REFERENCES

Albrecht, R., Barbieri, C., Adorf, H.-M., Corrain, G., Gemmo, A., Greenfield, P., Hainaut, O., Hook, R. N., Tholen, D. J., Blades, J. C., and Sparks, W. B. 1994. High-resolution imaging of the Pluto-Charon system with the Faint Object Camera of the Hubble Space Telescope. *Astrophys. J. Lett.* 435:75–78.

Binzel, R. P. 1988. Hemispherical color differences on Pluto and Charon. *Science* 241:1070–1072.

Buie, M. W., and Tholen, D. J. 1989. The surface albedo distribution of Pluto. *Icarus* 79:23–27.

Buie, M. W., Tholen, D. J., and Horne, K. 1992. Albedo maps of Pluto and Charon: Initial mutual event results. *Icarus* 97:211–227.

Buie, M. W., Tholen, D. J., and Wasserman, L. H. 1996. Separate lightcurves of Pluto and Charon. *Icarus*, submitted.

Cruikshank, D. P., Pilcher, C. B., and Morrison, D. 1976. Pluto: Evidence for methane frost. *Science* 194:835–837.

Drish, W. F., Jr., Harmon, R., Marcialis, R. L., and Wild, W. J. 1995. Images of Pluto generated by matrix lightcurve inversion. *Icarus* 133:360–386.

Eaton, J. A., and Hall, D. S. 1979. Starspots as the cause of the intrinsic light variations in RS Canum Venaticorum type stars. *Astrophys. J.* 227:907–922.

Hansen, C. J. 1994. Seasonal Nitrogen Cycles on Triton and Pluto. Ph.D. Thesis, Univ. of California, Los Angeles.

Hapke, B. 1981. Bidirectional reflectance spectroscopy. *J. Geophys. Res.* 86:3039–3054.

James, F., and Roos, M. 1975. MINUIT—a system for function minimization and analysis of the parameter errors and correlations. *Comput. Phys. Commun.* 10:343.

Marcialis, R. L. 1983. A Two Spot Model for the Surface of Pluto. Master's Thesis, Vanderbilt University.

Morrison, D., Jones, T. J., Cruikshank, D. P., and Murphy, R. E. 1975. The two faces of Iapetus. *Icarus* 24:157–171.

Owen, T. C., Roush, T. L., Cruikshank, D. P., Elliot, J. L., Young, L. A., de Bergh, C., Schmitt, B., Geballe, T. R., Brown, R. H., and Bartholomew, M. J. 1993. Surface ices and the atmospheric composition of Pluto. *Science* 261:745–748.

Reinsch, K., Burwitz, V., and Festou, M. C. 1994. Albedo maps of Pluto and improved physical parameters of the Pluto–Charon system. *Icarus* 108:209–218.

Russell, H. N. 1906. On the light-variations of asteroids and satellites. *Astrophys. J.* 24:1–18.

Stern, S. A., Trafton, L. M., and Gladstone, G. R. 1988. Why is Pluto bright? Implications of the albedo and lightcurve behavior of Pluto. *Icarus* 75:485–498.

Stern, S. A., Buie, M. W., and Trafton, L. M. 1996. Global imaging of Pluto with the Hubble Space Telescope. *Science*, in preparation.

Young, E. F., and Binzel, R. P. 1993. Comparative mapping of Pluto's sub-Charon hemisphere: Three least squares models based on mutual event lightcurves. *Icarus* 102:134–149.

PLUTO AND CHARON

S. Alan Stern
David J. Tholen

Editors

With the editorial assistance of
A. S. Ruskin, M. L. Guerrieri and M. S. Matthews

With 50 collaborating authors

THE UNIVERSITY OF ARIZONA PRESS
Tucson